

Experimental validation of pore-scale models for gas diffusion layers

Liusheng Xiao^a, Lijun Zhu^b, Christian Clökler^d, Alex Grünzweig^d, Florian Wilhelm^d, Joachim Scholta^d, Roswitha Zeis^e, Zu-Guo Shen^b, Maji Luo^{b,c,**}, Pang-Chieh Sui^{b,c,*}

^a Ningbo University, Faculty of Maritime and Transportation, 315211, Ningbo, China

^b Wuhan University of Technology, School of Automotive Engineering, 430070, Wuhan, China

^c Foshan Xianhu Laboratory of the Advanced Energy Science and Technology Guangdong Laboratory, 528000, Foshan, China

^d Zentrum für Sonnenenergie- und Wasserstoff-Forschung, 89071, Ulm, Germany

^e Karlsruhe Institute of Technology, Helmholtz Institute Ulm, 89081, Ulm, Germany

HIGHLIGHTS

- GDL reconstruction under various compression ratios is conducted.
- 3D deformation of GDL is investigated experimentally and numerically.
- Effect of compression on anisotropic transport properties for GDL is studied.
- Pore-scale modeling is validated by experimental data.

ARTICLE INFO

Keywords:

Gas diffusion layer
Pore-scale modeling
Transport properties
X-ray computed tomography
Conductivity measurements

ABSTRACT

Pore-scale modeling developed over the past decades has become a powerful method to evaluate the effective transport properties of porous electrodes. Experimental verification for such a method is crucial to confirm the method's validity. In this study, experimental data of gas diffusion layer (GDL) are compared with results of pore-scale modeling. GDL microstructures are scanned and reconstructed by X-ray computed tomography. Explicit dynamic simulations based on the finite element method are performed on these reconstructed models to reveal the 3D displacement of the microstructure during compression. Over the deformed models, the effective diffusivity, thermal and electrical conductivities are then computed using a pore-scale model code. It is found that, as the compression ratio increases to 30%, the fiber displacement increases obviously with significant anisotropy, and the fibers gradually squeeze into nearby pores located in the adjacent layers inside GDL. The effective diffusivity and permeability decrease by about 15% and 35% respectively. The conductivity increases by 100% and 20% in the through-plane and in-plane direction respectively. Compared with the empirical model, the pore-scale models are in better agreement with the experiments. The validated methods can support microstructure optimization and transport properties improvement for different types of porous electrodes.

1. Introduction

Vehicles powered by proton exchange membrane fuel cells (PEMFCs) are considered a promising future because of their advantages of high efficiency, zero emissions, short refueling time, low noise, and long driving mileage. The hardware of a typical PEMFC is made of two major components, i.e., the bipolar plates and the membrane electrode assembly (MEA). The bipolar plates facilitate the transfer of reactants, product water, electricity, and heat to or from the MEA. The gas

diffusion layer (GDL) is one of the core components of the MEA, where oxygen, hydrogen, and water are transported through its pores, and electrons and heat are conducted through its solid materials. Due to the complex microstructure, it is challenging to predict the effective transport properties of GDL accurately. The microstructure deformation caused by the assembly force exerted through the bipolar plates may significantly affect local transport properties such as diffusivity, thermal conductivity, and electrical conductivity, which further impacts the overall performance of PEMFCs. The understanding of compression

* Corresponding author. Wuhan University of Technology, School of Automotive Engineering, 430070, Wuhan, China.

** Corresponding author. Wuhan University of Technology, School of Automotive Engineering, 430070, Wuhan, China.

E-mail addresses: mjluo@whut.edu.cn (M. Luo), pcsui@whut.edu.cn (P.-C. Sui).

force on GDL performance is thus crucial to the optimal design and operation of PEMFC.

GDL is typically composed of carbon fiber, binder, and Polytetrafluoroethylene (PTFE). Fibers are mainly distributed along the in-plane (IP) direction; binder and PTFE are coated and bonded with carbon fibers. The transport properties in the through-plane (TP) and IP directions are usually quite different because of the anisotropic microstructure inside GDLs. A few researchers have experimentally studied the effect of compression on the microstructure change [1–5], polarization curve [6], stress-strain distributions [7], GDL thermal conductivity [8], and the pressure distribution between the bipolar plate (BPP) and GDL [9]. In-situ characterization techniques and operando characterization techniques [10–12] were comprehensively summarized.

Due to the high cost of experiments, numerical modeling and simulation have been proposed as alternative approaches. With numerical methods, the macro-scale, inhomogeneous deformation of GDL and its effects on PEMFC performance [13], pressure distribution [14], contact resistance [15], GDL porosity, GDL permeability [15–17], current density, and polarization curve [18], were analyzed. These works were based on the macro-scale formulation, not reflecting the real microstructure change. A few new methods that attempt to solve the transport at the length scale of the pores and solid fibers have been developed to address this drawback, e.g., see Mukherjee et al. [19,20]. Several methods can be used for pore-scale modeling (PSM), e.g., finite element method (FEM) [7,21], finite volume method (FVM) [22,23], and lattice Boltzmann method (LBM) [24,25]. FEM is usually used for solid mechanics simulation, FVM is commonly applied to calculate the transport of species and charge, and LBM is normally used for two-phase flow modeling.

PSM was applied to reveal the microstructure change under compression and evaluate its effects on transport properties for GDLs [26,27]. The Three-dimensional (3D) GDL model was reconstructed at pore-scale firstly. Compression simulation was conducted to obtain the compressed models, which are finally used to investigate their transport properties under different compression ratios (CR). Espinoza et al. [28] and Schulz et al. [29] simulated the compression process of GDL microstructure by assuming that there is only a parallel movement of carbon fibers during compression. However, they ignored the bending, arching, dynamic contact, frictional motion, and extrusion deformation among fibers. Gaiselmann et al. [30] used a vector matrix to represent the new position of compressed carbon fibers and validated the result with experiments. However, the results were only accurate in the TP direction but not valid in the IP direction. On the other hand, after the GDLs were compressed, the GDL transport properties, such as the diffusivity [31], the permeability [32], the thermal conductivity [33], and electrical resistivity [34] at different CRs were investigated experimentally [35–39] and numerically at pore-scale [7,21,40–42]. LBM was employed to simulate the permeability of two-dimensional (2D) compressed GDLs, which assumed that two crossing fibers of adjacent layers could penetrate each other [43]. The parallel movement of carbon fibers was considered during compression for 2D [28], and 3D [44] compressed GDLs, ignoring the bending and extruding phenomenon among carbon fibers. It is noted that these assumptions cannot ensure the accuracy of subsequently computed transport properties. Therefore, Xiao et al. conducted the solid mechanics simulation and pore-scale modeling to calculate the diffusivity and the conductivity [7,40] of GDL at different CRs, which is more accurate and objective by considering the dynamic contact, friction, extrude, and bending phenomenon among fibers in both TP and IP directions during compression. Nevertheless, experimental validation of these numerical works is lacking.

Validated pore-scale models can improve the fidelity to predict and evaluate the potential impact on the effective transport properties of porous electrodes. To this end, experimental techniques including X-ray computed tomography (XCT) and electrical and thermal conductivities were employed in the present study. The data are compared with

numerical results obtained from pore-scale simulations. This study aims to validate the methodology of pore-scale modeling on GDL's microstructural change under compression and to evaluate its effect on the transport properties with higher accuracy.

2. Experimental methods

This section describes experimental methods, including XCT, compression tests, thermal conductivity, and electrical resistivity measurements. Fig. 1 shows the workflow of the current approach. XCT was employed to scan the GDL sample and reconstruct its 3D model at CR 0%. After that, the XCT model was meshed into the FEM model; then, solid mechanics simulation was performed on the FEM model to obtain the compressed GDL model at different CRs. These GDL models were then exported for PSM modeling to calculate the effective transport properties, including the gas diffusivity, the thermal conductivity, and the electrical conductivity. Compression tests and XCT were also carried out to characterize the GDL microstructure, such as the local porosity, pore size distribution, and 2D cross-sectional microstructure at different CRs, which were used to validate the FEM results. Besides, to validate the PSM results, the thermal conductivity and electrical resistivity of compressed GDL samples were measured.

2.1. X-ray computed tomography

XCT combined with the compression setup was employed to compress, scan, reconstruct and characterize the 3D GDL microstructure at different CRs, see Fig. 2. The experiments were completed in Zentrum für Sonnenenergie und Wasserstoff-Forschung (ZSW), Germany. The XCT images were captured by the Skyscan 1172 desktop device with an energy level of 36 kV and a source current of 222 μ A [45]. The 2D greyscale images were obtained by scanning the GDL sample (SGL GDL 39AA, produced by SIGRACELL® company, Germany) with the rotating step of 0.2° and the resolution of 2.99 μ m. These images were further used for thresholding and reconstruction to the 3D GDL model by NRECON® software (Bruker Corp) and AVIZO software. The diameter of the sample is 9 mm. The GDL sample and the compression setup are enclosed in the XCT machine when running, as shown in Fig. 2 (a). Therefore, the compression setup is controlled by the computer, and the compression speed is set as 5 μ m/s.

2.2. Thermal conductivity and electrical resistivity measurements

Conductivity experiments and compression tests were carried out to measure the thermal and electrical conductivity of GDL samples in the IP and TP directions at different CRs. The CR was controlled by Zwick Roell Prüfmaschine 5 kN with a compression rate of 0.28 mm/min (or 4.6 μ m/s) during each compression step, see Fig. 3. At each set value, a 30-min stabilization time was given. The conductivity measurements were performed in ZSW, Germany [46]. The thermal resistance ($K \cdot W^{-1}$) of the GDL sample can be calculated from the temperature difference and heat flux measured from the experiments:

$$R_T = \frac{\Delta T}{Q} \quad (1)$$

where ΔT is a temperature difference, and Q is the heat flux. The thermal conductivity ($W \cdot m^{-1} \cdot K^{-1}$) can be computed as:

$$\lambda = \frac{d}{R_T \cdot A} \quad (2)$$

where A is the projected surface area for TP direction and the cross-sectional area for IP direction, d is the thickness of the GDL sample (for TP direction) or the distance between probes (for IP direction).

The electrical resistivity of the GDL samples is measured by providing a current that passes through the samples. The voltage across

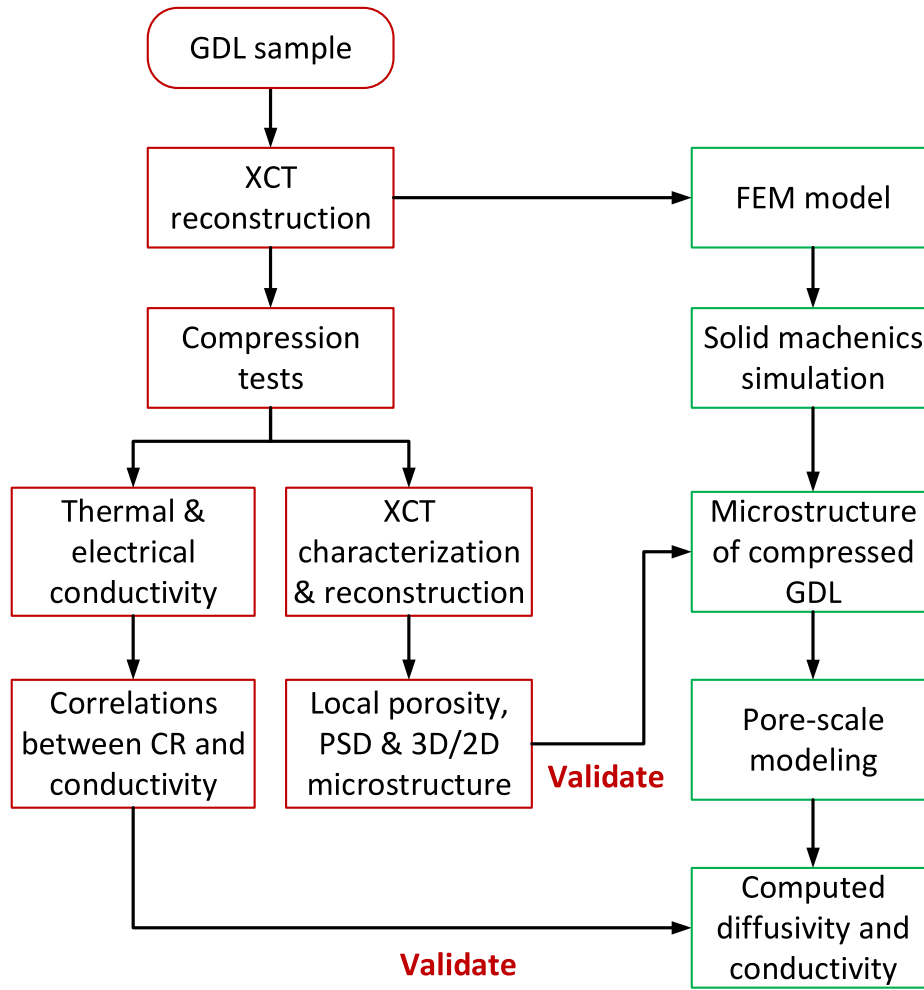


Fig. 1. Workflow of experimental validation of pore-scale modeling.

the sample is then measured using two gold-plated probes between two points on the path of the electrical current, see Fig. 3 (b). The electrical resistance of the GDL sample (Ω) can be calculated by the voltage and the current measured from the experiments:

$$R = \frac{U}{I} \quad (3)$$

where U is the voltage, and I is the current. The electrical resistivity ($\Omega \cdot m$) can be calculated as:

$$\rho = \frac{R \cdot A}{d} \quad (4)$$

3. Numerical methods

This section introduces numerical methods, including FEM and PSM, to calculate displacement distribution and transport properties of GDL microstructures under different CRs.

3.1. Finite element method

The FEM and the explicit dynamics theory were used to compute the displacement distributions in the TP and the IP directions of the meshed GDL model by considering the dynamic contact, friction, extruding, and bending among carbon fibers during compression. During the compression simulation, some assumptions were made, including the continuity, complete elasticity, homogeneity, and isotropic of the GDL materials. The governing equations of this compression simulation are

the kinematic equation, the geometric equation, and the physical equation.

Kinematic equations:

$$\sigma_{ij,j} + f_i = \rho u \quad (5)$$

where σ is the stress, ρ is the material density, f_i is the body force due to the clamping force, and u is the acceleration.

Geometric equations:

$$\varepsilon_{ij} = \frac{1}{2} (u_{i,j} + u_{j,i}) \quad (6)$$

where ε is the strain and u is the displacement.

Physical equations:

$$\begin{cases} \sigma_{ij} & \lambda \varepsilon_{kk} \delta_{ij} + 2\mu \varepsilon_{ij} \\ \sigma_{kk} & (3\lambda + 2\mu) \varepsilon_{kk} \end{cases} \quad (7)$$

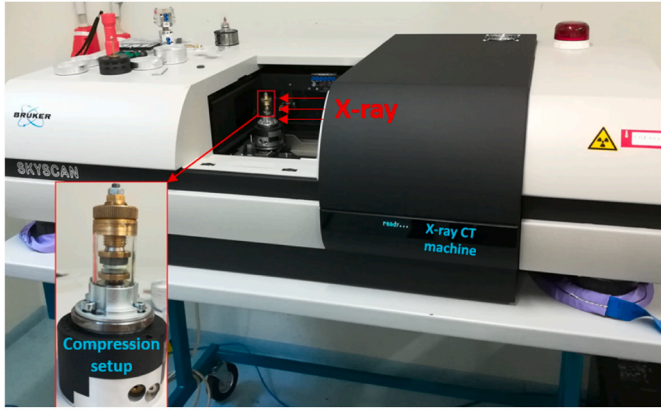
where λ and μ are the first and second Lamé constants of the material, respectively, and δ_{ij} is the Kronecher symbol.

Boundary conditions:

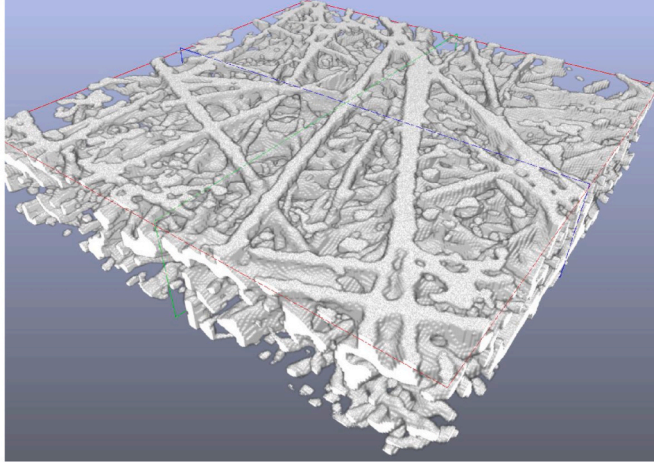
$$\begin{cases} u_i(x, t) & \bar{u}_i(x, t) \\ p_i(x, t) & \bar{p}_i(x, t) \end{cases} \quad (8)$$

where $\bar{u}_i(x, t)$, $\bar{p}_i(x, t)$ are displacement and stress boundary conditions, respectively.

The initial conditions:



(a)



(b)

Fig. 2. Experimental setup: (a) XCT setup and compression device (b) reconstructed 3D GDL model from XCT images.

$$\begin{cases} u(x, 0) & u_0(x) \\ u(x, t_1) & u_1(x) \end{cases} \quad (9)$$

where $u_0(x)$ and $u_1(x)$ are the given functions.

The boundary conditions (BCs), initial conditions (ICs), Hamilton's variation principle, and the central difference in time [47,48] are combined to solve the dynamic response of the simulation model. The 3D displacement of fibers can be calculated.

3.2. Pore-scale modeling

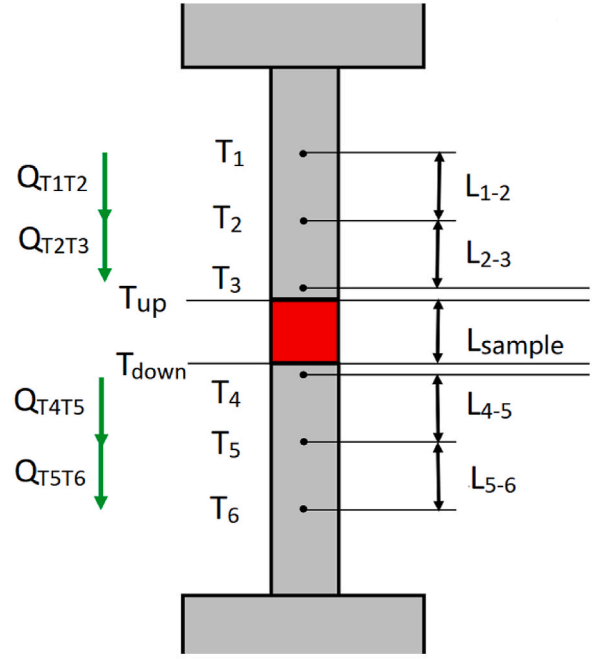
The PSM code reported in our previous studies [49–51] was employed to calculate the effective transport properties of the compressed GDL models obtained from the FEM simulations. The PSM code solves a complete set of conservation equations in the reconstructed domain. The transport of gas species, electricity, and heat occur essentially through the pores, fiber and binder materials, and the entire domain. The governing equations of pore-scale modeling are:

$$j_g = D_g \nabla c_g \quad (10)$$

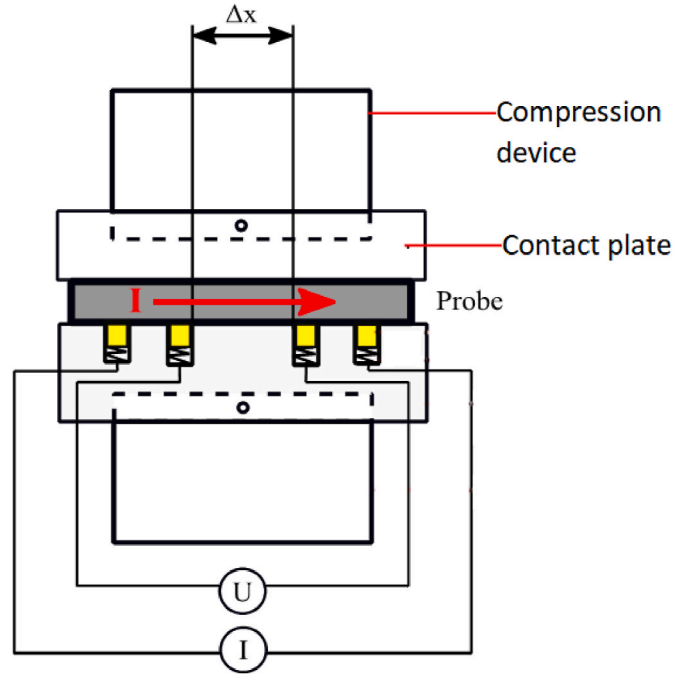
$$j_e = \sigma_e \nabla \varphi_e \quad (11)$$

$$j_T = \lambda_T \nabla T_T \quad (12)$$

where j_g , D_g , and c_g mean the flux, diffusivity, and concentration of gas species, respectively; j_e , σ_e , and φ_e mean the electrical flux, conductivity, and potential of the solid phase, respectively; and j_T , λ_T , and T_T mean the



(a)



(b)

Fig. 3. Experimental setups for (a) TP thermal conductivity and (b) IP electrical resistivity measurements.

thermal conductivity and temperature of the solid phase, respectively.

The conservation equations of gas species, electron, and thermal are:

$$\nabla \cdot j_g = 0 \quad (13)$$

$$\nabla \cdot j_e = 0 \quad (14)$$

$$\nabla \cdot j_T = 0 \quad (15)$$

To solve the above equations, the inlet and outlet ones are set as Dirichlet boundary conditions, and the remaining four boundaries are set as periodic conditions. The effective transport properties of the GDL are calculated from the fluxes obtained by the PSM as follows:

$$M_{eff} = \frac{j \cdot l}{b_2 - b_1} \quad (16)$$

where M_{eff} is the effective transport parameter, j is the flux calculated by the PSM simulation, l is the length of the computational domain, and b_1 , b_2 are the pre-described boundary conditions.

4. Results and discussion

This section investigates the effect of compression on the microstructural change of GDL at different CRs. The displacement distribution, slice porosity distribution, pore size distribution, and the 3D/2D microstructure of the simulation and experimental results are compared to evaluate the accuracy of FEM. Then the effect of compression on the transport properties by PSM is investigated, including the diffusivity, the thermal conductivity, and the electrical resistivity in the TP and IP directions. The TP thermal conductivity and the IP electrical resistivity of the modeling and experimental results are compared to validate the accuracy of PSM. The PSM and another empirical model are compared to evaluate the more accurate one.

The GDL model (domain: $X \times Y \times Z = 1002 \mu\text{m} \times 1002 \mu\text{m} \times 299 \mu\text{m}$) reconstructed from the XCT data is a 3D hollow surface model, which must be materialized to a solid geometry for further meshing. There are many potholes and sharp protrusions on the reconstructed fibers, making it highly challenging to mesh with high-quality that meets the requirement of explicit dynamics simulation. A smaller meshing size is used in the specific areas of overlap, contact, boundary, and stress concentration to ensure the unit connectivity and high meshing quality. The total meshing element is 9.6 million, see Fig. 4 (a). A mesh independence study was firstly conducted, from which the minimum element size was determined to be two μm , and the mesh size was chosen as one μm in this work, cf. our previous study [7]. The contact type between carbon fibers is set as the frictional contact to reflect the actual contact behavior between fibers. The contact points are automatically detected and tracked during the compression process, and penetration of fibers is not allowed. A fixed constraint that restricts all degrees of freedom is applied to the bottom of the model. A displacement constraint that only allows TP direction movement is used to the top of the model (zero displacement in the X and Y directions, and 90 μm displacement in the Z direction, corresponding to CR = 30%). Symmetry constraint is applied on all other surfaces. In the computational model, the fixed constraint is used on the carbon fibers that have been contacted before compression, while the frictional contact is applied on the carbon fibers that have not been contacted before compression. Fibers would contact each other during the compression, automatically and dynamically detected during the simulation. The FEM and the explicit dynamics method are used for solid mechanics simulation to study the displacement distribution of the GDL microstructure in both the TP and IP directions.

4.1. Effects of compression on fiber displacement

Large displacements of the carbon fibers occur in both the TP and IP directions during the compression. The fiber materials gradually squeeze into the nearby pores in the adjacent layers inside the GDL. As shown in Fig. 4(b)(c)(d), the displacement of carbon fibers in the X, Y and Z directions is in the ranges of $26 \sim +62 \mu\text{m}$, $91 \sim +50 \mu\text{m}$ and $23 \sim +132 \mu\text{m}$ respectively for the case with CR = 30%. For the displacement distribution in the Z direction, the positive values represent the downward direction (compression direction), and the negative values mean the upward direction. One can see that the displacement of

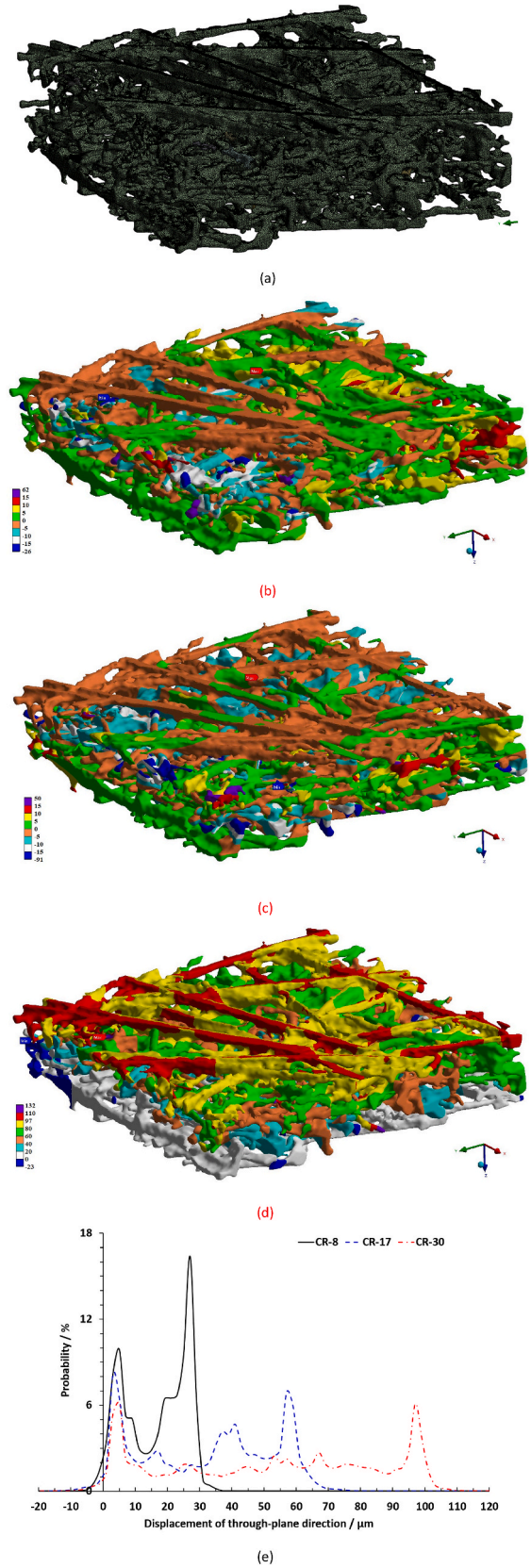


Fig. 4. (a) Model mesh, displacement distribution in (b) X direction, (c) Y direction, (d) Z direction, and (e) displacement probability in Z direction under CR = 8%, 17%, 30%.

the carbon fibers located in the top area is the highest, followed by the middle area and the bottom area shares the lowest displacement. If a solid material is in a stationary-state with the force and stress in an equilibrium, the entire domain should have similar deformation according to the law of action and reaction. However, for a GDL structure subjected to a dynamic compression, the body force-stress-momentum of the fiber material should be balanced, as explained in equation (5) according to the conservation of momentum. Therefore, as the compression force is applied from the top to the bottom of the GDL, the displacement of the fibers would depend on the velocity and acceleration of the fiber materials. The velocity of fiber element depends on the compression speed and the fiber's Young's modulus. In addition, since the microstructure of GDL is rather porous with a porosity about 0.8, the top area inside the GDL thus shows the highest displacement, whereas the bottom area shows the lowest, similar to what happens when a sponge is subjected to an external force. The area with higher density carbon fibers shows a much smaller displacement because more carbon materials contact and extrude each other, resulting in higher resistance to the microstructure movement. This study can reflect the real microstructural change more accurately during compression by considering the contact and extruding behaviors among fibers and the movement of fibers in the TP and IP directions. This is more realistic than some previous works [28–30,43], which only considered the downward displacement and parallel movement in the TP direction.

Fig. 4. (e) demonstrates the probability distribution of displacement in Z direction at different CRs. The probability in Fig. 4(e) for a given displacement value is computed by counting the number of fiber elements falling within a displacement interval (2 μm) and divided by the total mesh number of 9.6 million. It can be found that as the CR increases, the displacement ranges become wider, including the downward movement (positive value) and up-warping direction (negative value). The contact, bending, and extruding phenomena of carbon fibers become more obvious for $\text{CR} > 17\%$. The displacement range of CR 8% is $10 \sim +40 \mu\text{m}$, which increases to $15 \sim +80 \mu\text{m}$ for CR 17% and $20 \sim +120 \mu\text{m}$ for CR 30%. Besides, the probability distribution curve of the displacement moves to the downward and rightward directions with increasing CR, indicating that more carbon materials are compressed with higher displacement. As the CR increases from 8% to 17%, the probability between 0 and 30 μm is halved, while the probability between 30 and 70 μm increases dramatically. Several peaks and valleys (not evenly distributed) are experienced for the probability distribution curve.

To validate the FEM results, a comparison between the simulation results and experimental data based on XCT and microstructure characterization techniques is conducted. Fig. 5 shows the comparison between slice porosity distribution (SPD), pore size distribution (PSD) and tortuosity. The thickness of the GDL is 299 μm . The curves moving to the right direction means that the compression direction of the GDL is downward during the compression experiment. As shown in Fig. 5(a), a good agreement in the SPD is found between experimental data and simulation results. Slight deviations are noted that (1) the slice porosity of the structure near the top and bottom surfaces is higher for the simulation, (2) the probability of pore size $>70 \mu\text{m}$ is higher, and the probability of pore size $<60 \mu\text{m}$ is lower for the FEM models at different CRs, and (3) the tortuosity for the FEM models is slightly lower. This is expected because the air-noise microstructures, tiny particles, and sharp corner microstructures from the XCT models have been deleted or optimized to obtain a higher-quality FEM model. It can be seen from Fig. 5 (a) that there is a small degree of up-down fluctuations between the experimental and simulation curves. During the experiments, there was a 5-h wait to ensure carbon fibers were stable and static after every CR setting, which was not done in the FEM simulation due to computational time. Nevertheless, the deviation between the simulation and experiments is relatively tiny.

Fig. 6 shows the comparison of 2D slice microstructure at different thickness positions. Only the case of CR 17% is presented as an

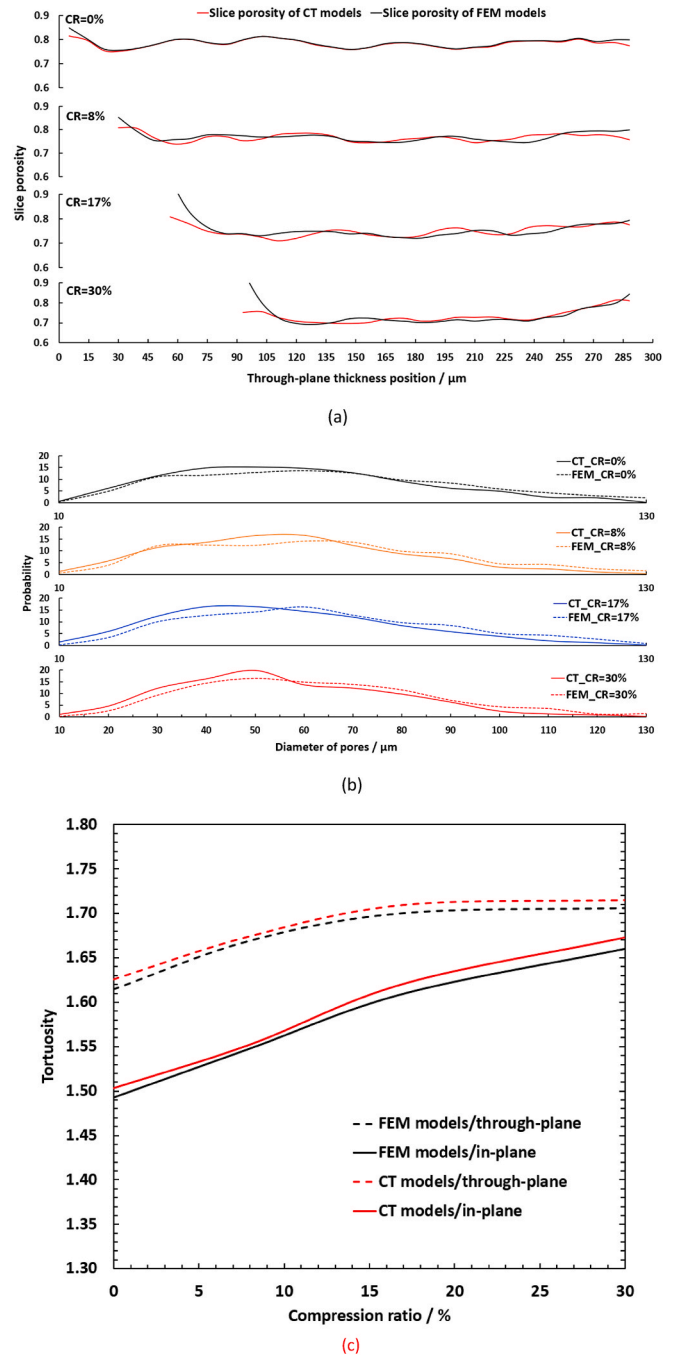


Fig. 5. Comparison between simulation and experiment results: (a) slice porosity distribution, (b) pore size distribution, and (c) tortuosity at different CRs.

example, and the thickness of this compressed GDL is 248 μm . According to the slice microstructures of thickness positions with 25 μm , 88 μm , and 190 μm , a conclusion is made that the simulation agrees well with experiments. The continuity of the 2D image represents the displacement deviation of carbon fibers in the TP direction, and the dislocation means the displacement deviation in the IP direction. In all, the displacement deviation is about 1–2%, indicating a good agreement between FEM results and XCT data.

4.2. Effects of compression on effective transport properties

The computed diffusivity, thermal conductivity, and electrical

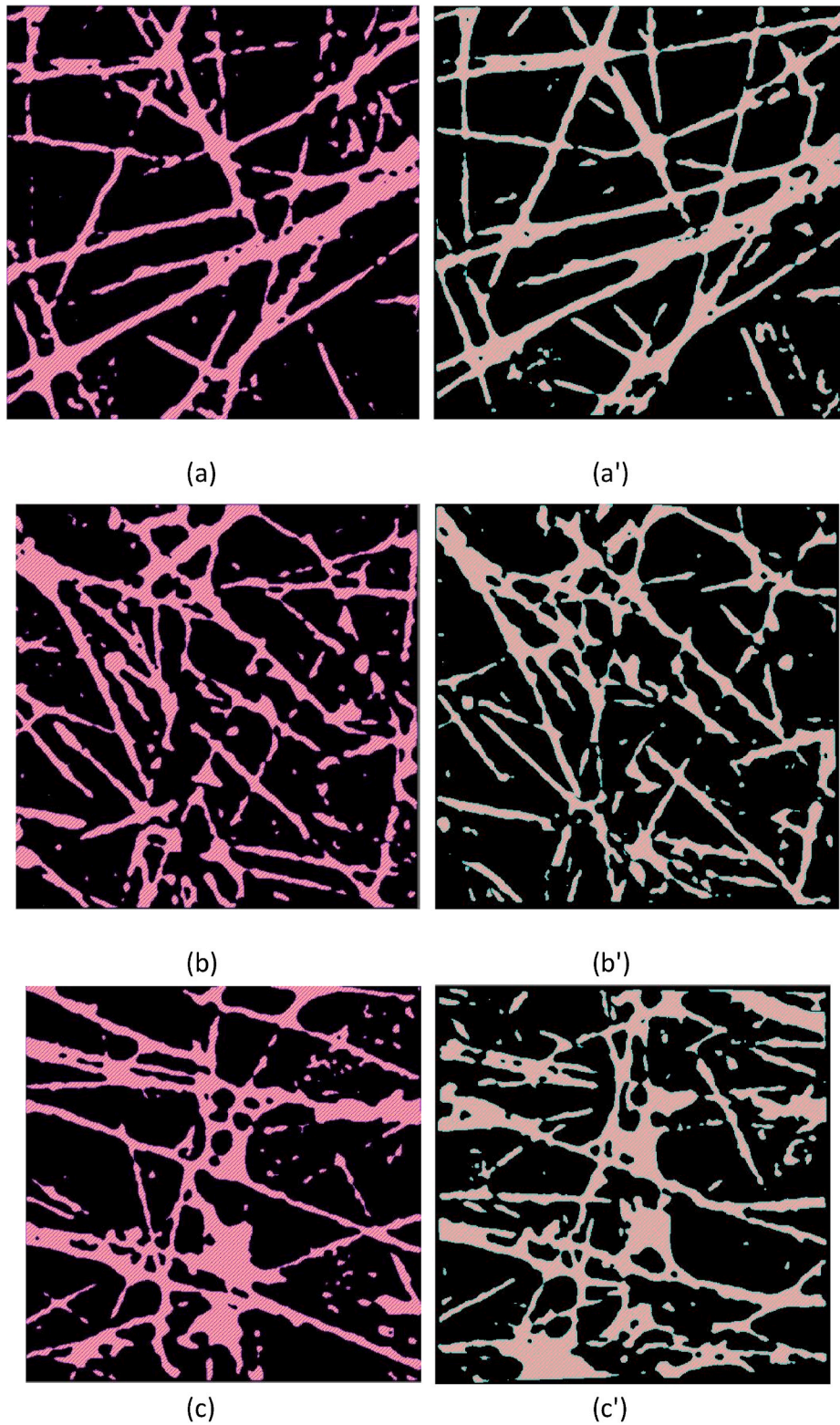


Fig. 6. 2D images of slice microstructure from experiment (left) and simulation (right): (a) & (a') thickness position with 25

resistivity are compared with experiments to validate the PSM code [49–51]. The models used for PSM are obtained from the GDL geometry in Section 4.1, which considers the contact-extruding-bending-3D deformation of fibers and pore size changes at different CRs.

From Fig. 7 (a), one can expect that the effective diffusivity would decrease with increasing CR because the connectivity and size of the

pores decreases, which results in higher resistance of gas transport. As CR increases to 30%, the effective diffusivity is decreased by 15.7% and 11.5% for the IP and TP directions, respectively. Fig. 7 (a) also shows that the effective diffusivity in the IP direction is higher than the TP direction. It is expected because the fiber orientation is mainly in the IP direction, resulting in more increased connectivity of pores and higher

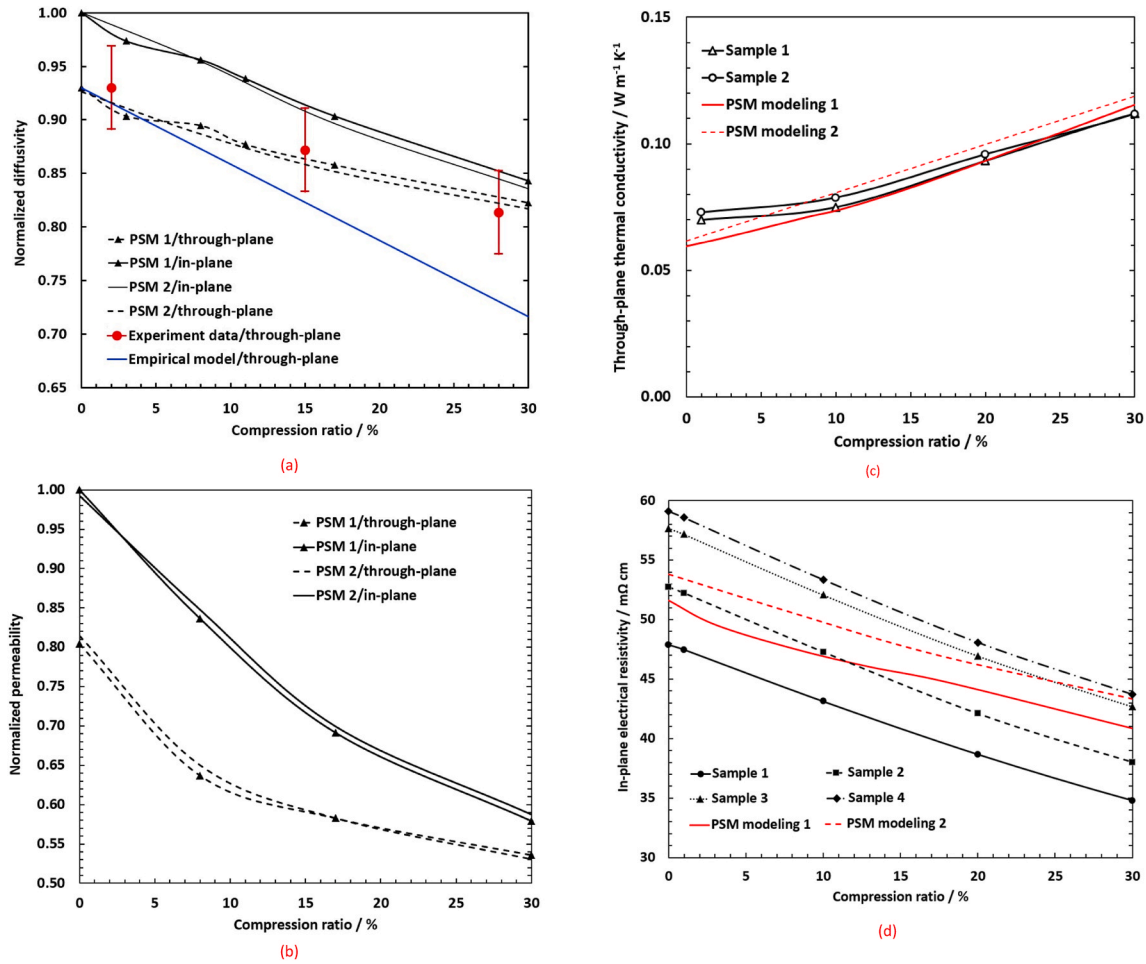


Fig. 7. (a) Normalized diffusivity in the IP and TP direction, (b) normalized permeability in the IP and TP direction, (c) thermal conductivity in the TP direction, and (d) electrical resistivity in the IP direction at different CRs.

continuity of carbon materials. As shown in Fig. 7 (a), the PSM results are compared with both experimental and empirical results. The results show that the PSM models are in good agreement with the experimental data [52], while there is a significant difference between the empirical model [53] and the experimental data. Opposite to the trend of effective diffusivity, the effective thermal and electrical conductivities increase simultaneously as CR increases. This is because the effective conductivity depends on the continuity of solid materials instead of pores.

Lattice Boltzmann method is used to calculate the effective permeability of GDLs at different CRs. Detailed descriptions of the governing and solving equations can be found in our previous work [25]. It can be seen from Fig. 7 (b) that the permeability decreases by 33% and 43% in the TP and IP direction respectively as the CR increases to 30%. This is because the fiber materials are extruded into the pores during compression. The pores are compressed to be smaller, and some pathways of gas are closed. The permeability of the IP direction is much higher than that of the TP direction because the fibers are mainly orientated in the IP direction. The difference of the permeability between the IP and TP directions decreases as the CR increases, indicating that the microstructure of the GDL becomes more isotropic.

Fig. 7(c)(d) compares the thermal conductivity and electrical resistivity of numerical and experimental results at different CRs. Two and four samples were prepared for thermal conductivity and electrical resistivity measurement, respectively. It was found that the measured electrical resistivity of four samples differed from each other over a noticeable range. It can be seen from Fig. 7 (c) that the thermal conductivity calculated by the PSM method increases by 101% in the TP

direction. The measured thermal conductivity of two samples in the TP direction increases linearly as the CR increases from 10% to 30%, yet the change is quite small as the CR increases from 1% to 10%. It is found that when the CR = 1%, the average deviation between the experiments and simulation is about 15.1%, while the average deviation is 1.3%, 0% and 2.7% for CR = 10%, 20% and 30%, respectively. The main reasons for the high deviation for the CR = 1% case are: (1) the measured data varies from different samples (tests) located in different areas; (2) the PSM model obtained from XCT data is different from the samples used in the conductivity measurement; (3) there could be uncertainties during the experiments of controlling the CR, especially when CR < 10%; (4) the contact thermal resistance depends on the contact points and the area. It is challenging to accurately evaluate and quantify the actual contact degree in the experimental samples when the CR is < 10%. Overall, the thermal conductivity of PSM is in good agreement with the experimental results.

The experimental measured electrical resistivity of four samples in the IP direction linearly decreases by about 26% (from about 55 mΩ·cm to 42 mΩ·cm) as the CR increases from 0% to 30%, see Fig. 7 (d), while the electrical resistivity computed by PSM decreases by 22.3% (from about 51.5 mΩ·cm to 40 mΩ·cm). The average deviation between the experiments and simulation is about 1.9%, 0%, 4.76% and 7.36% for CR = 0%, 10%, 20% and 30%, respectively. Therefore, the PSM results agree with the measurement well, and the deviation is acceptable. One can see the PSM simulations have variations within approximately 3–4% of the full scale. This is by no means a rigorous uncertainty analysis, but it gives us a sense of that the simulation results still fall within the range

of the experimental data.

4.3. Comparison between PSM and the empirical model

There have been some empirical correlations in the literature that quantify the relationship between effective transport properties and characteristics parameters of porous media [54] of a GDL. These correlations were obtained from experiments with an underlying assumption that the GDL isotropic. In the present study, a comparison of thermal conductivity between experimental data, PSM results, and an empirical model is conducted to evaluate the validity of the PSM approach. The empirical model [54] is expressed as:

$$\lambda = \frac{2\lambda_s \cdot (1 - \varepsilon)}{2 + \varepsilon} \quad (17)$$

where λ_s is the thermal conductivity of solid material, and ε is the porosity.

Fig. 8 compares the thermal conductivity obtained from PSM, the empirical model, and the present experiments. One can see that the thermal conductivity calculated by the empirical correlation differs significantly from the experimental results, while that computed by PSM based on anisotropic GDL microstructure is in good agreement with the experimental data. As CR increases, the deviation between the empirical model and the experimental data increases significantly, while the PSM results are much closer to the experimental results at different CRs. The difference between the empirical model and PSM results increases as CR increases. It can be seen from Fig. 8 that the difference is significant under low compressions. This is because the surface of the real GDL sample is not absolutely flat, resulting in a half or partial contact between the GDL samples and the contact plate under very low compression ratios during the experiments. On the other hand, the surfaces of GDL models are reconstructed to be absolutely flat, leading to the difference under low compression ratios. It is noted that GDLs fabricated by other companies may have drastically different microstructures. Therefore, to predict the transport properties of GDL more accurately, the current PSM approach that considers real GDL geometry and the deformation of fibrous materials is preferred.

Nevertheless, for engineering applications, a correlation equation the GDL case tested can be curve-fitted to predict the thermal conductivity. Based on the PSM results and experimental data, the effective thermal conductivity in the TP direction for the SGL type GDL is estimated as:

$$\lambda = \lambda_s \cdot e^{2.2 \cdot CR} \quad (18)$$

where λ_s indicates the thermal conductivity of the uncompressed GDL, and CR means the compression ratio.

5. Conclusions

In this paper, XCT imaging, thermal-electrical conductivity measurements, and pore-scale simulations are carried out to investigate the effects of compression on GDL's microstructural deformation and the effective transport properties. The experiments are conducted to validate these pore-scale models, and the simulation results are compared with the existing empirical model. It is found that the present pore-scale modeling can accurately calculate the 3D displacement distribution, the diffusivity, and the thermal-electrical conductivity of GDL microstructure, which provides strong support for subsequent microstructure improvement and transport properties optimization for different types of the porous electrode. The main conclusions are:

- (1) The displacement of carbon fibers in the X, Y and Z directions is in the ranges of 26 ~ +62 μm , 91 ~ +50 μm and 23 ~ +132 μm respectively with CR = 30%. Carbon fibers' displacement in the IP and TP directions increases significantly, and the fiber

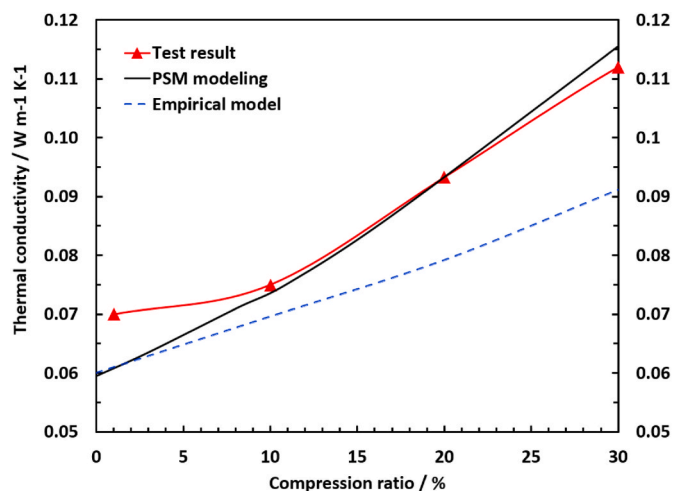


Fig. 8. Comparison of thermal conductivity among PSM, empirical model, and test.

materials gradually squeeze into the nearby pores located in the adjacent layers inside GDL as the CR increases.

- (2) As CR increases to 30%, the effective diffusivity decreases by about 15% in the TP and IP directions, the effective permeability decreases by 33% and 43% in the TP and IP directions, the effective thermal conductivity in the TP direction increases by 101%, and the effective electrical resistivity in the IP direction decreases by 22%, showing that the conductivity in the TP direction is more sensitive.
- (3) The TP thermal conductivity computed by PSM based on the real-anisotropic GDL microstructures is in good agreement with the experiment, which is more accurate than the empirical model by considering the 3D movement and displacement of fiber materials.

CRedit authorship contribution statement

Liusheng Xiao: Conceptualization, Methodology, Formal analysis, Data curation, Writing – original draft. **Lijun Zhu:** Formal analysis, Data curation, Writing – original draft. **Christian Clokler** and **Alex Grünzweig:** Preparation and operation for experiments. **Florian Wilhelm** and **Joachim Scholta:** Guidance for experiments. **Roswitha Zeis:** Funding acquisition, Experimental conditions providing. **Zu-Guo Shen:** Writing – review & editing. **Maji Luo:** Supervision, Writing – review & editing. **Pang-Chieh Sui:** Supervision, Funding acquisition, Writing – review & editing.

Declaration of competing interest

The authors declare that they have no known competing financial interests or personal relationships that could have appeared to influence the work reported in this paper.

Acknowledgments

The authors gratefully acknowledge financial support from China's National Natural Science Foundation (No. 52106254 and 21776226), the Foshan Xianhu Laboratory of the Advanced Energy Science and Technology Guangdong Laboratory (XHD2020-004), and Chinesisch-Deutsche Zentrum für Wissenschaftsförderung (M-0070). This work contributes to the research performed at CELEST (Center for Electrochemical Energy Storage Ulm-Karlsruhe).

References

- [1] N. Khajeh-Hosseini-Dalasm, T. Sasabe, T. Tokumasu, U. Pasaogullari, Effects of polytetrafluoroethylene treatment and compression on gas diffusion layer microstructure using high-resolution X-ray computed tomography, *J. Power Sources* 266 (2014) 213–221.
- [2] C. Totzke, G. Gaiselmann, M. Osenberg, J. Bohner, T. Arlt, H. Markotter, et al., Three-dimensional study of compressed gas diffusion layers using synchrotron X-ray imaging, *J. Power Sources* 253 (2014) 123–131.
- [3] C. Totzke, I. Manke, G. Gaiselmann, J. Bohner, B.R. Muller, A. Kupsch, et al., A dedicated compression device for high resolution X-ray tomography of compressed gas diffusion layers, *Rev. Sci. Instrum.* 86 (2015), 043702.
- [4] I.V. Zenyuk, D.Y. Parkinson, L.G. Connolly, A.Z. Weber, Gas-diffusion-layer structural properties under compression via X-ray tomography, *J. Power Sources* 328 (2016) 364–376.
- [5] C. Totzke, G. Gaiselmann, M. Osenberg, T. Arlt, H. Markotter, A. Hilger, et al., Influence of hydrophobic treatment on the structure of compressed gas diffusion layers, *J. Power Sources* 324 (2016) 625–636.
- [6] J.-H. Lin, W.-H. Chen, Y.-J. Su, T.-H. Ko, Effect of gas diffusion layer compression on the performance in a proton exchange membrane fuel cell, *Fuel* 87 (2008) 2420–2424.
- [7] L. Xiao, M. Luo, H. Zhang, R. Zeis, P.-C. Sui, Solid mechanics simulation of reconstructed gas diffusion layers for PEMFCs, *J. Electrochem. Soc.* 166 (2019) F377–F385.
- [8] I. Nitta, O. Himanen, M. Mikkola, Thermal conductivity and contact resistance of compressed gas diffusion layer of PEM fuel cell, *Fuel Cell* 8 (2008) 111–119.
- [9] J.d.I. Cruz, U. Cano, T. Romero, Simulation and in situ measurement of stress distribution in a polymer electrolyte membrane fuel cell stack, *J. Power Sources* 329 (2016) 273–280.
- [10] E.M. Khetabi, K. Bouziane, N. Zamel, X. François, Y. Meyer, D. Candusso, Effects of mechanical compression on the performance of polymer electrolyte fuel cells and analysis through in-situ characterisation techniques - a review, *J. Power Sources* 424 (2019) 8–26.
- [11] Q. Meyer, Y. Zeng, C. Zhao, In situ and operando characterization of proton exchange membrane fuel cells, *Adv. Mater.* 31 (2019), e1901900.
- [12] A. Ozden, S. Shahgaldi, X. Li, F. Hamdullahpur, A review of gas diffusion layers for proton exchange membrane fuel cells—with a focus on characteristics, characterization techniques, materials and designs, *Prog. Energy Combust. Sci.* 74 (2019) 50–102.
- [13] H. Zhang, L. Xiao, P.-Y.A. Chuang, N. Djilali, P.-C. Sui, Coupled stress–strain and transport in proton exchange membrane fuel cell with metallic bipolar plates, *Appl. Energy* 251 (2019) 113316.
- [14] L. Peng, D. Qiu, P. Yi, X. Lai, An analytical model for contact pressure prediction considering dimensional error of stamped bipolar plate and gas diffusion layer in proton exchange membrane fuel cell stack assembly, *J. Electrochem. Energy Convers. Stor.* (2016) 13.
- [15] P. Zhou, C.W. Wu, Numerical study on the compression effect of gas diffusion layer on PEMFC performance, *J. Power Sources* 170 (2007) 93–100.
- [16] Z.Y. Su, C.T. Liu, H.P. Chang, C.H. Li, K.J. Huang, P.C. Sui, A numerical investigation of the effects of compression force on PEM fuel cell performance, *J. Power Sources* 183 (2008) 182–192.
- [17] Y. Zhou, K. Jiao, Q. Du, Y. Yin, X. Li, Gas diffusion layer deformation and its effect on the transport characteristics and performance of proton exchange membrane fuel cell, *Int. J. Hydrogen Energy* 38 (2013) 12891–12903.
- [18] I. Nitta, S. Karvonen, O. Himanen, M. Mikkola, Modelling the effect of inhomogeneous compression of GDL on local transport phenomena in a PEM fuel cell, *Fuel Cell* 8 (2008) 410–421.
- [19] P.P. Mukherjee, C.-Y. Wang, Q. Kang, Mesoscopic modeling of two-phase behavior and flooding phenomena in polymer electrolyte fuel cells, *Electrochim. Acta* 54 (2009) 6861–6875.
- [20] P.P. Mukherjee, Q. Kang, C.-Y. Wang, Pore-scale modeling of two-phase transport in polymer electrolyte fuel cells—progress and perspective, *Energy Environ. Sci.* 4 (2011) 346–369.
- [21] X. Zhou, Z. Niu, Z. Bao, J. Wang, Z. Liu, Y. Yin, et al., Two-phase flow in compressed gas diffusion layer: finite element and volume of fluid modeling, *J. Power Sources* 437 (2019) 226933.
- [22] D. Maggiolo, F. Zanini, F. Picano, A. Trovò, S. Carmignato, M. Guarnieri, Particle based method and X-ray computed tomography for pore-scale flow characterization in VRFB electrodes, *Energy Storage Mater.* 16 (2019) 91–96.
- [23] H. Zhang, L. Zhu, H.B. Harandi, K. Duan, R. Zeis, P.-C. Sui, et al., Microstructure reconstruction of the gas diffusion layer and analyses of the anisotropic transport properties, *Energy Convers. Manag.* 241 (2021) 114293.
- [24] L. Chen, H.-B. Luan, Y.-L. He, W.-Q. Tao, Pore-scale flow and mass transport in gas diffusion layer of proton exchange membrane fuel cell with interdigitated flow fields, *Int. J. Therm. Sci.* 51 (2012) 132–144.
- [25] K. Duan, L. Zhu, M. Li, L. Xiao, N. Bevilacqua, L. Eifert, et al., Multiphase and pore scale modeling on catalyst layer of high-temperature polymer electrolyte membrane fuel cell, *J. Electrochem. Soc.* 168 (2021).
- [26] V. Norouzfard, M. Bahrami, Deformation of PEM fuel cell gas diffusion layers under compressive loading: an analytical approach, *J. Power Sources* 264 (2014) 92–99.
- [27] G. Inoue, K. Yokoyama, J. Ooyama, T. Terao, T. Tokunaga, N. Kubo, et al., Theoretical examination of effective oxygen diffusion coefficient and electrical conductivity of polymer electrolyte fuel cell porous components, *J. Power Sources* 327 (2016) 610–621.
- [28] M. Espinoza, M. Andersson, J. Yuan, B. Sundén, Compress effects on porosity, gas-phase tortuosity, and gas permeability in a simulated PEM gas diffusion layer, *Int. J. Energy Res.* 39 (2015) 1528–1536.
- [29] V.P. Schulz, J. Becker, A. Wiegmann, P.P. Mukherjee, C.Y. Wang, Modeling of two-phase behavior in the gas diffusion medium of PEMFCs via full morphology approach, *J. Electrochem. Soc.* 154 (2007) B419–B26.
- [30] G. Gaiselmann, C. Totzke, I. Manke, W. Lehnert, V. Schmidt, 3D microstructure modeling of compressed fiber-based materials, *J. Power Sources* 257 (2014) 52–64.
- [31] L. Zhu, W. Yang, L. Xiao, H. Zhang, X. Gao, P.-C. Sui, Stochastically modeled gas diffusion layers: effects of binder and polytetrafluoroethylene on effective gas diffusivity, *J. Electrochem. Soc.* 168 (2021), 014514.
- [32] H. Zhang, L. Zhu, H.B. Harandi, K. Duan, R. Zeis, P.-C. Sui, et al., Microstructure reconstruction of the gas diffusion layer and analyses of the anisotropic transport properties, *Energy Convers. Manag.* (2021) 241.
- [33] H. Zhang, M.A. Rahman, F. Mojica, P.C. Sui, P.Y.A. Chuang, A comprehensive two-phase proton exchange membrane fuel cell model coupled with anisotropic properties and mechanical deformation of the gas diffusion layer, *Electrochim. Acta* 382 (2021).
- [34] L. Zhu, H. Zhang, L. Xiao, A. Bazylak, X. Gao, P.-C. Sui, Pore-scale modeling of gas diffusion layers: effects of compression on transport properties, *J. Power Sources* (2021) 496.
- [35] D. Todd, M. Schwager, W. Merida, Three-dimensional anisotropic electrical resistivity of PEM fuel cell transport layers as functions of compressive strain, *J. Electrochem. Soc.* 162 (2015) F265–F272.
- [36] P. Roy Chowdhury, A. Vikram, R.K. Phillips, M. Hoorfar, Measurement of effective bulk and contact resistance of gas diffusion layer under inhomogeneous compression – Part II: thermal conductivity, *J. Power Sources* 320 (2016) 222–230.
- [37] A. Vikram, P.R. Chowdhury, R.K. Phillips, M. Hoorfar, Measurement of effective bulk and contact resistance of gas diffusion layer under inhomogeneous compression - Part I: electrical conductivity, *J. Power Sources* 320 (2016) 274–285.
- [38] M. Taş, G. Elden, An Experimental Investigation of the Effects of Operating Conditions on Anisotropic Electrical Conductivity in a PEM Fuel Cell, *Fuel Cells*, 2020.
- [39] N. Kulkarni, M.D.R. Kok, R. Jervis, F. Iacoviello, Q. Meyer, P.R. Shearing, et al., The effect of non-uniform compression and flow-field arrangements on membrane electrode assemblies - X-ray computed tomography characterisation and effective parameter determination, *J. Power Sources* 426 (2019) 97–110.
- [40] L. Xiao, M. Luo, L. Zhu, K. Duan, N. Bevilacqua, L. Eifert, et al., Pore-scale characterization and simulation of porous electrode material for vanadium redox flow battery: effects of compression on transport properties, *J. Electrochem. Soc.* 167 (2020) 110545–110554.
- [41] S. Simaafrookhteh, R. Taherian, M. Shakeri, Stochastic microstructure reconstruction of a Binder/Carbon Fiber/Expanded graphite carbon fiber paper for PEMFCs applications mass transport and conductivity properties, *J. Electrochem. Soc.* 166 (2019) F3287–F3299.
- [42] Z. Tayarani-Yoosefabad, D. Harvey, J. Bellerive, E. Kjeang, Stochastic microstructural modeling of fuel cell gas diffusion layers and numerical determination of transport properties in different liquid water saturation levels, *J. Power Sources* 303 (2016) 208–221.
- [43] D. Froning, J. Brinkmann, U. Reimer, V. Schmidt, W. Lehnert, D. Stolten, 3D analysis, modeling and simulation of transport processes in compressed fibrous microstructures, using the Lattice Boltzmann method, *Electrochim. Acta* 110 (2013) 325–334.
- [44] G.R. Molaeimanesh, M. Nazemian, Investigation of GDL compression effects on the performance of a PEM fuel cell cathode by lattice Boltzmann method, *J. Power Sources* 359 (2017) 494–506.
- [45] R. Banerjee, S. Chevalier, H. Liu, J. Lee, R. Yip, K. Han, et al., A comparison of felt-type and paper-type gas diffusion layers for polymer electrolyte membrane fuel cell applications using X-ray techniques, *J. Electrochem. Energy Convers. Stor.* (2017) 15.
- [46] R. Banerjee, N. Bevilacqua, A. Mohseninia, B. Wiedemann, F. Wilhelm, J. Scholta, et al., Carbon felt electrodes for redox flow battery: impact of compression on transport properties, *J. Energy Storage* 26 (2019) 100997.
- [47] G. Herbert, P. Charles, S. John, *Classical Mechanics*, Addison Wesley, United States of America, 1980.
- [48] S.R. Wu, L. Gu, *Introduction to the Explicit Finite Element Method for Nonlinear Transient Dynamics*, Library of Congress Cataloging in Publication Data, United States of America, 2012.
- [49] K.J. Lange, P.-C. Sui, N. Djilali, Determination of effective transport properties in a PEMFC catalyst layer using different reconstruction algorithms, *J. Power Sources* 208 (2012) 354–365.
- [50] K.J. Lange, P.-C. Sui, N. Djilali, Pore scale modeling of a proton exchange membrane fuel cell catalyst layer: effects of water vapor and temperature, *J. Power Sources* 196 (2011) 3195–3203.
- [51] K.J. Lange, P.-C. Sui, N. Djilali, Pore scale simulation of transport and electrochemical reactions in reconstructed PEMFC catalyst layers, *J. Electrochem. Soc.* 157 (10) (2010) B1434–B1442.
- [52] R. Flückiger, S.A. Freunberger, D. Kramer, A. Wokaun, G.G. Scherer, F.N. Büchi, Anisotropic, effective diffusivity of porous gas diffusion layer materials for PEFC, *Electrochim. Acta* 54 (2008) 551–559.
- [53] T. Rosén, J. Eller, J. Kang, N.I. Prasianakis, J. Mantzaras, F.N. Büchi, Saturation dependent effective transport properties of PEFC gas diffusion layers, *J. Electrochem. Soc.* 159 (2012) F536–F544.
- [54] P.H. Chi, S.H. Chan, F.B. Weng, A. Su, P.C. Sui, N. Djilali, On the effects of non-uniform property distribution due to compression in the gas diffusion layer of a PEMFC, *Int. J. Hydrogen Energy* 35 (2010) 2936–2948.